Optics Letters

Widefield quantitative polarized light microscopy using spectrally encoded null polarimetry

Hugo Laviec, Matthieu Dubreuil,* Sylvain Rivet, Mikhail Indenbom, and Yann Le Grand

Univ. of Brest, Laboratory of Optics and Magnetism OPTIMAG UR 938, F-29200 Brest, France
**matthieu.dubreuil@univ-brest.fr*

Received 15 July 2024; revised 23 August 2024; accepted 23 August 2024; posted 27 August 2024; published 6 September 2024

Quantitative polarized light microscopy enables determination of optical retardation and azimuth of birefringent specimens and is a powerful tool for label-free imaging in the fields of biology and pathology. We have recently proposed a device for fast laser-scanning birefringence microscopy based on a near-infrared wavelength-swept laser and spectral encoding of polarization, resulting in a channeled spectrum generated during the wavelength-sweep of the laser and highly sensitive to optical retardation [Opt. Lett. 49, 387 (2024)]. In this Letter, we propose its transposition to visible widefield imaging using a white light source and a high-order retarder for spectral encoding and a hyperspectral camera to record the channeled spectrum at each point of the image in parallel. The method proposed here allows for straightforward conversion of any widefield microscope into a highly sensitive and quantitative polarized light microscope. © 2024 Optica Publishing Group. All rights, including for text and data mining (TDM), Artificial Intelligence (AI) training, and similar technologies, are reserved.

https://doi.org/10.1364/OL.536534

Quantitative polarized light microscopy consists in acquiring 2D maps of optical retardation δ (nm) and azimuth α (°) associated with linear birefringence induced by a specimen and is used in biology and pathology to reveal optically anisotropic structures without labeling [1]. Indeed, several macromolecular assemblies, such as collagen fibers, exhibit linear birefringence due to their molecular order (intrinsic birefringence) and/or shape (form birefringence). Usually, optical retardation within a thin biological specimen observed under a transmission polarized light microscope is weak and challenging to detect. Many implementations of quantitative birefringence microscopy were proposed based on different methods that share advantages and drawbacks in terms of sensitivity, accuracy, spatial resolution, speed, and ease of integration. They can be classified in two categories: off-null and null methods. Off-null methods are based on illumination with various polarization states distributed all around the Poincaré sphere and often lack sensitivity because they require the detection of a small change in light intensity against a very intense background, which rapidly saturates the photodetector and limits the signal-to-noise ratio. Null methods work close to extinction by illuminating the specimen with polarization states located around a pole of the Poincaré sphere, enabling higher illumination power on the sample while detecting optical signals on an almost zero light background, which prevents saturation of the detector and boosts the sensitivity. A small angle bias has to be introduced to move away from pure extinction in order to linearize the optical retardation measurement. The most popular setup based on this principle is the LC-PolScope developed by M. Shribak and R. Oldenbourg in the 2000s, allowing acquisition of optical retardation and azimuth images in a widefield configuration with liquid-crystal-based active modulators [2].

Our team has developed several techniques for polarization sensing based on spectral encoding of light polarization [3–5]. The spectral encoding process is made possible by the strong chromaticity of high-order retarders. The detection requires a spectral analysis to demodulate polarization features from a channeled spectrum [6–8]. We have recently proposed a method based on null polarimetry enabling optical retardation measurement at high speed and with high sensitivity [5] and have implemented this method for single-scan laser-scanning birefringence microscopy [9]. Nevertheless, quantitative polarized light microscopy is predominantly employed in a widefield configuration. In [5,9], spectral analysis was transposed to time using a fast wavelength-swept laser. However, this strategy is not transposable to widefield microscopes.

In this Letter, we propose, to our knowledge, a novel configuration for widefield sensitive quantitative birefringence microscopy based on a white light source and a high-order retarder for spectral encoding of polarization and a hyperspectral camera for spectral analysis and imaging. This setup enables highly sensitive acquisition of the diffraction-limited optical retardation and azimuth images without any active elements. This method can be easily implemented in any widefield microscope by replacing the traditional camera with a hyperspectral camera and inserting compact and passive components in the optical path of the microscope.

A schematic of the setup is shown in Fig. 1(a) and built around a transmission light upright microscope (Zeiss, Axioskop II). It is composed of a halogen source, a polarization state generator (PSG) itself composed of a polarizer, a high-order retarder (HOR), and a polymer zero-order quarter-wave plate at 532 nm. The specimen is incoherently illuminated in a Köhler configuration by a condenser of variable numerical aperture. Between

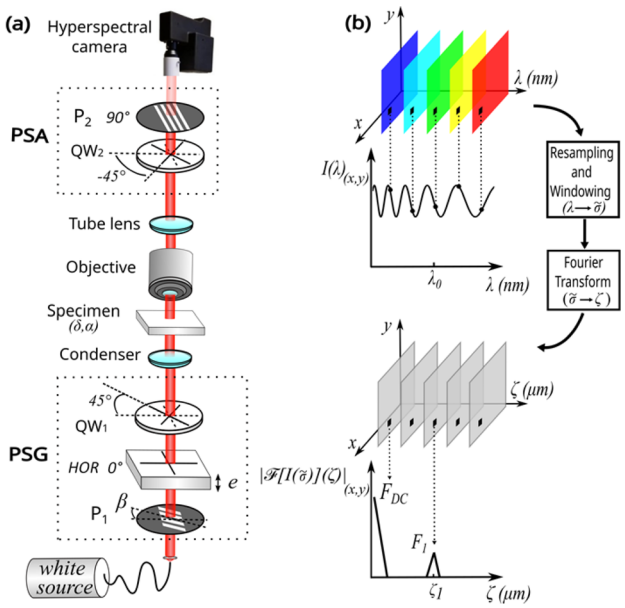

Fig. 1. (a) Setup for widefield quantitative polarized light microscopy. PSG, polarization state generator; PSA, polarization state analyzer; P_1 and P_2, linear polarizers oriented, respectively, at β (bias angle) and 90°. The 0° is the horizontal direction. QW_1 and QW_2, quarter-wave plates oriented, respectively, at 45° and −45°; *HOR*, high-order retarder of thickness e oriented at 0°. (b) Workflow of post-processing for the calculation of optical retardation δ and azimuth α at central wavelength λ_0 from a hyperspectral datacube (x,y,λ).

the tube lens and the hyperspectral camera, a second polymer zero-order quarter-wave plate at 532 nm and an analyzer oriented at 90° form a polarization state analyzer (PSA). Polymer zero-order quarter-wave plates were chosen according to their high acceptance angle for imaging and high spectral acceptance to act as an achromatic quarter-wave plate within the analyzing window. They are oriented at +45° and −45° from the 0° position determined by the input polarizer in order to generate and analyze a set of polarization states close to circular and to work close to extinction. The input polarizer is rotated by a small bias angle β from the crossed position in order to slightly move away from extinction (null configuration). The HOR, made of quartz of birefringence $\Delta n = 0.009$ and thickness $e = 2$ mm, is aligned with the 0° position. The image is formed on the CCD sensor of a hyperspectral camera (4200 M, HinaLea Imaging).

The λ-scan of the camera is generated by an internal scanning Fabry–Perot filter to obtain hyperspectral datacubes (x,y,λ) in the range 400–1000 nm with 300 equally spaced spectral channels. Each spectral image has a full resolution of 968×608 pixels. The spectral resolution of the hyperspectral camera is 4 nm (FWHM) with a spectral sampling of 2 nm. An IR filter is set before the camera to block light above 800 nm which is out of the specifications of visible polarizers and can induce overexposure of the camera in the 800–1000 nm region. Inter-band switching time is about 2 ms and exposure time τ for each spectral channel was set around 400 ms depending on the specimen. The total acquisition time $T_{acq} = N_c \tau$ of a hyperspectral datacube thus mostly depends on the exposure time τ and the number of channels N_c rather than the inter-band switching.

For each pixel with spatial coordinates (x,y), the spectrum $I_{(x,y)}(\lambda)$ is processed to calculate $\delta_{(x,y)}$ and $\alpha_{(x,y)}$. Hereafter the case of weak optical retardation measurements is considered, and expressions will be given at the first order approximation in δ. The theoretical spectrum can be calculated using Jones formalism and written as a function of wavenumber $\tilde{\sigma} = 1/\lambda$:

$$I_{(x,y)}(\tilde{\sigma}) = I_0 T \sin^2(\beta) + I_0 T \frac{\pi}{\lambda_0} \delta_{(x,y)} \sin(2\beta) \cos(2\alpha_{(x,y)} + 2\pi \Delta n e \tilde{\sigma}) \quad (1)$$

with λ_0 the central wavelength of the analyzing window, Δn the birefringence of the HOR of thickness e, T the transmittance of the specimen, and I_0 the incident power on the specimen. The dependence of I_0 and T on the wavenumber was not displayed for simplicity. Equation (1) assumes the optical retardation δ of the specimen to be negligible compared to the optical path difference $\mathrm{OPD} = \Delta n e$ of the HOR. In the presence of birefringence ($\delta \neq 0$), the spectrum $I(\tilde{\sigma})$ is a channeled spectrum containing a continuous term $I_{DC} = I_0 T \sin^2(\beta)$ and a modulation term at $\zeta_1 = \Delta n e$ which is related to the OPD of the HOR. The optical retardation δ and azimuth α are encoded in the modulation amplitude and phase, respectively. The discrete Fourier transform of the channeled spectrum leads to the following expressions for the complex Fourier peaks:

$$F_{DC} = \rho I_0 T \sin^2(\beta) \quad (2)$$

$$F_1 = \rho I_0 T \frac{\pi}{2\lambda_0} \delta \sin(2\beta) e^{j2\alpha} \quad (3)$$

with $j^2 = -1$ and ρ is a factor accounting for the detector responsivity and the number of sampling points (equal to the number of spectral channels N_c). One should note that the Fourier peak F_1 is proportional to the optical retardation, which guarantees good sensitivity for weak value measurements. The role of the bias angle β is to move away from pure extinction ($\beta = 0°$) because in that case the expression of I_{DC} would have to be evaluated at the second order in δ that would lead to the classical δ^2 quadratic dependence of the detected power which is not favorable in the case of weak measurements. In order to calculate the values of δ and α, a complex ratio γ between the two Fourier peaks is computed, allowing to free from the dependence with I_0 and T. This ratio is given by

$$\gamma = \frac{F_1}{F_{DC}} = \frac{\pi}{\lambda_0} \frac{\delta}{\tan(\beta)} e^{j2\alpha}. \quad (4)$$

From this ratio, the values of δ and α can be calculated independently by taking the modulus and the argument of γ, respectively. The values obtained for δ and α are mean values at the central wavelength λ_0 assuming that δ does not vary significantly over the spectral analyzing window.

As stated previously, the technique is based on the Fourier analysis of the spectrum $I_{(x,y)}(\lambda)$ at each pixel of the image to acquire a map $(\delta,\alpha)_{(x,y)}$ of the specimen linear birefringence. We here describe the multiple steps of the signal processing performed before the ratio γ is computed. The whole signal processing framework was written in Matlab R2019b. Firstly, the spectrum presents a chirp, because of the $1/\lambda$ dependence of the retardance induced by the HOR (Fig. 2(a)). The spectrum was thus first resampled according to the wavenumber $\tilde{\sigma}$ using the *resample* function of Matlab with the linear interpolation method (Fig. 2(b)). Then, the spectrum is truncated to an entire number of periods before Fourier transformation. In addition, because of the spectral envelope of the source, our signal presents a spectral leakage that can be reduced by using a window function. The choice of this window function must take into consideration

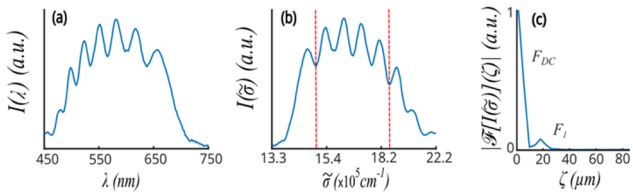

Fig. 2. Experimental data for one pixel of an image corresponding to a birefringent area. (a) Raw spectrum, represented in the 450–750 nm region. (b) Spectrum after resampling in wavenumber. The red dotted square indicates the truncation of the spectrum before Fourier transformation. (c) Norm of Fourier peaks after resampling, truncation, and windowing (Hamming) of the raw spectrum.

the proximity of the F_{DC} and F_1 peaks to avoid any overlap (Fig. 2(c)). The Hamming window was identified as most robust function to limit errors.

The finite spectral resolution of the hyperspectral camera results in a loss of contrast in the modulation. Furthermore, the resampled spectrum was subjected to a windowing operation prior to Fourier transformation. The combined effect of these two factors is a reduction in the amplitude of the F_1 peak, which is referred to as the drop-off effect. This issue can be resolved by artificially enhancing the amplitude of the F_1 peak through the application of a pre-determined correcting factor, which is established without specimen by setting the input polarizer at $\beta = 0°$ and the HOR at 45°. Indeed, in such a configuration, equivalent to setting a HOR at 45° between crossed polarizers, the amplitude of the F_1 peak should be half of the F_{DC} peak in the case of the infinite spectral resolution. The ratio of experimental and theoretical amplitudes is the correcting factor, equal to 1.25 here.

The OPD of the HOR has to be chosen according to the spectral width of the analysis window. Indeed, for a given analysis window, the number of periods depends on this OPD. For these experiments, a HOR made of quartz of birefringence $\Delta n = 0.009$ and of thickness $e = 2$ mm was used that leads to an 18 μm OPD. The analysis window was set between 543 and 674 nm, which results in four periods for the modulation sampled by $N_c = 66$ spectral channels around the central wavelength $\lambda_0 = 608$ nm. This choice appeared as a good compromise to guarantee (i) a good achromaticity of the zero-order quarter-wave plates, (ii) a sufficiently high modulation to prevent an overlap between F_1 and F_{DC} peaks, (iii) a sufficiently low modulation to be moderately affected by the drop-off.

In order to evaluate the detection limit of the instrument and show the interest of working close to extinction, a noise analysis is described for one pixel in terms of the standard deviation σ_{n_e} of the number of electrons n_e generated during the exposure time τ by [5]

$$\sigma_{n_e} = \sqrt{\frac{RI_{DC}}{q}\tau + \frac{i_D}{q}\tau + \sigma_r^2}, \tag{5}$$

where I_{DC} (W) is the continuous part of the channeled spectrum, q (C) is the unit charge, R (A/W) is the camera responsivity supposed constant over the analyzing window, i_D (A) is the dark current and σ_r^2 is the read noise of the camera expressed in number of electrons. The first term in Eq. (5) represents the shot noise and dominates while working close to the saturation level of the camera. The detection limit is defined as the standard deviation σ_δ of the optical retardation δ in a non-birefringent zone of the image. From Eq. (4), the standard deviation of δ can be written $\sigma_\delta = \frac{\lambda_0}{\pi}\tan(\beta)\sigma_{|\gamma|}$ where the standard deviation of $|\gamma|$ can be obtained by $(\sigma_{|\gamma|}/|\gamma|)^2 = (\sigma_{|F_1|}/|F_1|)^2 + (\sigma_{|DC|}/|F_{DC}|)^2$. Under the condition $|F_1| \ll |F_{DC}|$ (small optical retardation) and $\sigma_{|F_1|} = \sigma_{|DC|}$ (uncorrelated peaks), the second term of the right side is negligible and the detection limit is given by

$$\sigma_\delta = \frac{\lambda_0}{\pi}\tan(\beta)\frac{\sigma_{|F_1|}}{|F_{DC}|}. \tag{6}$$

As Eq. (6) involves $\sigma_{|F_1|}$ we need to consider noise in the Fourier space which is related to noise in the direct space by $\sigma_{F_1} = \sqrt{N_c}\sigma_{n_e}$. However, the detection limit is obtained from $\sigma_{|F_1|}$ that is related to σ_{F_1}, assuming a Rayleigh distribution [10], by $\sigma_{|F_1|} = \sigma_{F_1}\sqrt{(4-\pi)}/2$. In the shot noise limited regime considered here, σ_δ can be written using Eq. (5):

$$\sigma_\delta = \frac{\lambda_0}{2\pi\cos(\beta)}\sqrt{\frac{(4-\pi)q}{RN_cI_0T\tau}}. \tag{7}$$

To maximize the detection sensitivity, the parameters I_0, β, and the exposure time per channel τ must be chosen so that the maximal value of the spectrum approaches the saturation level of the camera. In particular, the lower the bias angle β the lower the detection limit, which justifies the necessity to work close to extinction in a quasi-null configuration. To satisfy this condition, one can set the maximal power I_0 and a low bias angle β; the saturation is reached by adjusting the exposure time per spectral channel τ.

In addition to the shot noise, other sources of errors, referred as systematic, can limit the sensitivity and the accuracy of the measurement. These errors mainly originate from the non-ideal compensation of the quarter-wave plates and their alignment [11]. To eliminate the contribution of these systematic errors, a background subtraction method is employed [11], which consists of acquiring a hyperspectral datacube without any specimen on the microscope stage, leading to the calculation of the ratio γ_{BG} for each pixel. The values of δ and α are in fact calculated using a corrected ratio γ_c defined as $\gamma_c = \gamma - \gamma_{BG}$.

To highlight our technique, in Fig. 3 is presented a quantitative birefringence image of a rotifer *Keratella cochlearis*. Figure 3(a) displays the optical retardation image, which highlights birefringent areas within the specimen. To evaluate the experimental detection limit of the technique, the standard deviation σ_δ over the pixels within the red square in a non-birefringent zone of the

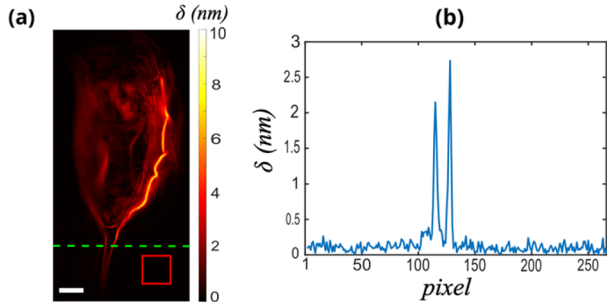

Fig. 3. (a) Optical retardation image of a rotifer *Keratella cochlearis*. The red square identifies the non-birefringent region in which the standard deviation was calculated to evaluate the detection limit. Image: 266 × 486 pixels. Microscope objective: 40×/0.95 NA. Exposure time per channel $\tau = 430$ ms. Bias angle $\beta = 10°$. Scale bar: 30 μm. (b) Line profile of optical retardation along the green dotted line of (a).

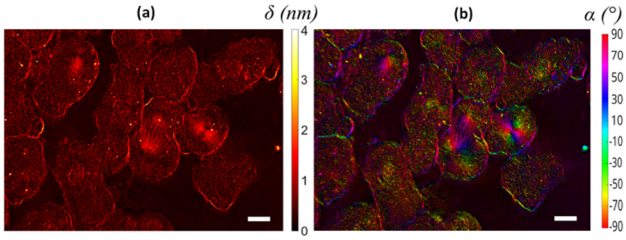

Fig. 4. (a) Optical retardation image and (b) azimuth image of a fixed sample containing whitefish blastomeres at different stages of mitosis. The azimuth image is encoded in the HSV space where the Hue was associated with the azimuth, the saturation was set to 1, and the value was associated with the optical retardation. Image: 968×608 pixels. Microscope objective: water immersion 60×/1.2 NA. Exposure time per channel $\tau = 420$ ms. Bias angle $\beta = 10°$. Scale bar: 10 µm.

image was calculated. This results in $\sigma_\delta = 0.045$ nm according to the following experimental parameters: $I_0 = 1.25$ nW/pixel, $\beta = 10°$, $N_c = 66$ channels and $\tau = 430$ ms. The theoretical value can be easily calculated by expressing σ_δ with the digital signal given by the camera I_{det} and its relative intensity noise $\sigma_{I_{det}}/I_{det}$, knowing that $\sigma_{F_1}/F_{DC} = (1/\sqrt{N_C}).(\sigma_{I_{\text{det}}}/I_{\text{det}})$, according to

$$\sigma_\delta = \frac{\lambda_0}{2\pi}\tan(\beta)\sqrt{\frac{(4-\pi)}{N_c}}\frac{\sigma_{I_{\text{det}}}}{I_{\text{det}}}. \quad \textbf{(8)}$$

With a measured relative intensity noise $\sigma_{I_{\text{det}}}/I_{\text{det}} = 2.1\%$, the theoretical value of σ_δ is then equal to 0.041 nm and is close to the experimental value; the difference can be attributed to drop-off that tends to increase the noise in the Fourier space. In Fig. 3(b), a line profile along the green line in Fig. 3(a) highlights the possibility to detect small variations in optical retardation.

In order to illustrate the performance of the instrument to image small optical retardation at the cellular scale, a fixed sample containing whitefish blastomeres at different stages of mitosis was imaged (Fig. 4). In addition to the optical retardation image presented in Fig. 4(a), the azimuth image was also displayed in Fig. 4(b) in order to facilitate the visualization of the orientation of birefringent structures within cells. It is evident that cells at varying stages of mitosis can be discerned. The most pronounced optical retardation signal emanates from microtubules, and the azimuth image offers dependable insight into microtubule organization and alignment during mitosis. Notably, information regarding the orientation of microtubules can be obtained at the earliest stages of metaphase.

In conclusion, we have proposed a novel configuration for quantitative birefringence microscopy, comprising a white light source and a high-order retarder for spectral encoding, and a hyperspectral camera for spectral analysis and imaging. The optical retardation and azimuth are encoded into a modulation of a channeled spectrum, which can then be demodulated with relative ease through the application of Fourier analysis. The detection limit for optical retardation was 0.045 nm, equivalent to λ/12,000 with the current experimental setup, and is comparable to the most advanced results obtained in wide-field quantitative polarized light microscopy. The concept of null polarimetry offers potential for reducing the detection limit through two avenues: (i) increasing the illumination power and lowering the bias angle at a fixed exposure time or (ii) increasing exposure time and lowering the bias angle at a fixed illumination power. This imaging modality can be implemented on any transmission light microscope by replacing the camera with a hyperspectral camera and inserting passive and compact components in the optical path of the microscope. This represents a novel application for hyperspectral cameras that will benefit from recent advances in this technology, particularly with regard to acquisition time and detection sensitivity [12].

Funding. Conseil Général du Finistère, Région Bretagne.

Acknowledgment. The authors thank G. Le Roux for technical assistance and E. Quemeneur for providing whitefish cell samples.

Disclosures. The authors declare no conflicts of interest.

Data availability. Data underlying the results presented in this paper are not publicly available at this time but may be obtained from the authors upon reasonable request.

REFERENCES

1. M. Koike-Tani, T. Tani, S. B. Mehta, *et al.*, Mol. Reprod. Dev. **82**, 548 (2015).
2. M. Shribak and R. Oldenbourg, Appl. Opt. **42**, 3009 (2003).
3. M. Dubreuil, S. Rivet, B. Le Jeune, *et al.*, Opt. Express **15**, 13660 (2007).
4. A. Le Gratiet, S. Rivet, M. Dubreuil, *et al.*, Opt. Lett. **40**, 645 (2015).
5. X. Theillier, S. Rivet, M. Dubreuil, *et al.*, Opt. Express **30**, 18889 (2022).
6. K. H. Nordsieck, PASP **86**, 324 (1974).
7. K. Oka and T. Kato, Opt. Lett. **24**, 1475 (1999).
8. F. J. Iannarilli Jr., S. H. Jones, H. E. Scott, *et al.*, *Proc. SPIE 3698, Infrared Technology and Applications XXV* (1999).
9. X. Theillier, S. Rivet, M. Dubreuil, *et al.*, Opt. Lett. **49**, 387 (2024).
10. K. Krishnamoorthy, *Handbook of Statistical Distributions with Applications* (Chapman and Hall/CRC, 2006).
11. X. Theillier, S. Rivet, M. Dubreuil, *et al.*, Appl. Opt. **62**, 7529 (2023).
12. M. Yako, Y. Yamaoka, T. Kiyohara, *et al.*, Nat. Photonics **17**, 218 (2023).